Electronic Supplementary Information (ESI) for *"Cold plasma activated CO_2 desorption from calcium carbonate for carbon capture"*

HONGTAO ZHONG[1], DANIEL PIRIAEI[1], GENNARO LICCARDO[2], JIEUN KANG[1], BENJAMIN WANG[1], MATTEO CARGNELLO[2], AND MARK A. CAPPELLI[1]

[1] Department of M echanical Engineering, Stanford University, Stanford, CA 94305, US
[2] Department of Chemical Engineering, Stanford University, Stanford, CA 94305, US

Corresponding E-mail: hongtaoz@stanford.edu

CONTENTS

1. EXPERIMENTAL SECTION

Details of the reactor system, deposited energy, species calibrations, optical diagnostics, measurement uncertainty, and material preparation methods are provided in this section.

A. Experimental Layout of the Plasma Reactor

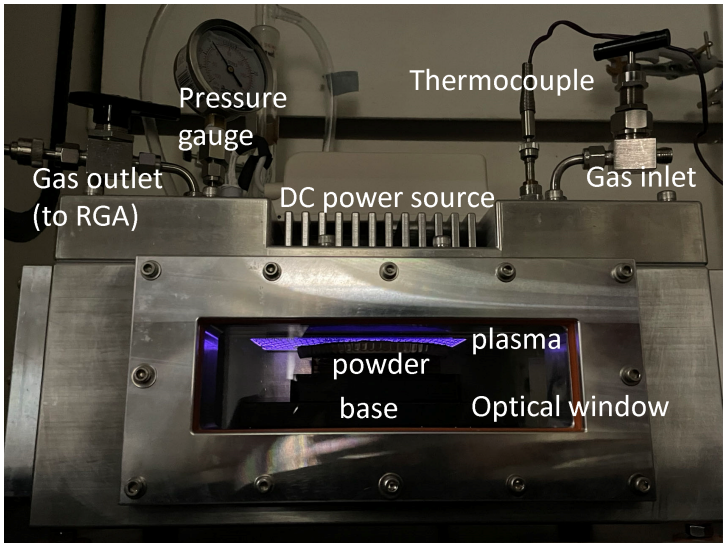

Fig. S1. Experimental layout of the plasma reactor.

The surface dielectric barrier discharge source consists of a flat high-voltage electrode, a buried electrode, and a dielectric layer sandwiched between the two electrodes, and chamber, as shown in Fig. S1. The dielectric layer is an alumina ceramic sheet. The size of the high voltage electrode is 10 cm $\times$ 15 cm, and the corresponding discharge area is 150 cm^2. The chamber is a 33 cm $\times$ 21 cm $\times$ 10 cm cube made of aluminium. A thermocouple and a pressure gauge were placed inside the gas chamber to measure the internal thermodynamic conditions. The high-voltage electrode is connected to a sinusoidal power supply. The experimental layout of the sDBD configuration is shown in Fig. S2. The bath gas flowing into the chamber was controlled by a mass flow meter and the composition was monitored downstream with a Residual Gas Analyzer (RGA). Inside the chamber, carbon capture material is placed in an aluminium base. The optical window is made of quartz, allowing the transmittance of UV light and UV-Vis absorption spectroscopy.

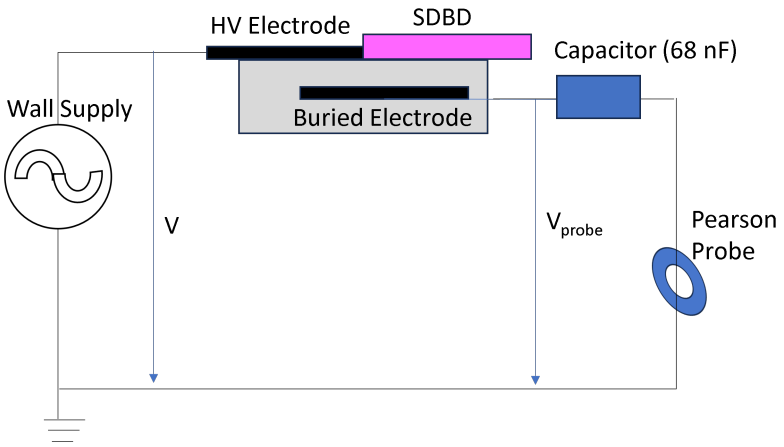

Fig. S2. Experimental layout and diagnostics for the customized sDBD configuration.

B. Plasma Deposited Energy Measurements

The evaluation of the area inside a Lissajous plot is a well-known method [1, 2] for evaluating the power consumed by the surface DBD fed with a sinusoidal high voltage difference. The Lissajous plot is obtained by plotting the charge flowing into the circuit Q as a function of the voltage difference ΔV between the electrodes. In this work, the charge is measured using a capacitor in series with the discharge cell (known as "capacitive probe").

Three electric probes have been used for studying the discharge properties as shown in Fig. S2. Two high-voltage probes (Tektronix P6015) were employed for evaluating the voltage at the HV electrode (V) and the voltage of the capacitor (V_{probe}), as shown in Fig. S3. The sinusoidal voltage waveform has been modulated. A capacitive probe ($C_{probe} = 68nF$) was placed between the buried electrode and the earth as a diagnostic for measuring power consumption and visualising the Lissajous figures' shapes. The outputs of all these probes were connected to different channels of a large bandwidth digital oscilloscope (Rigol, DS1104Z) and their signals were acquired simultaneously.

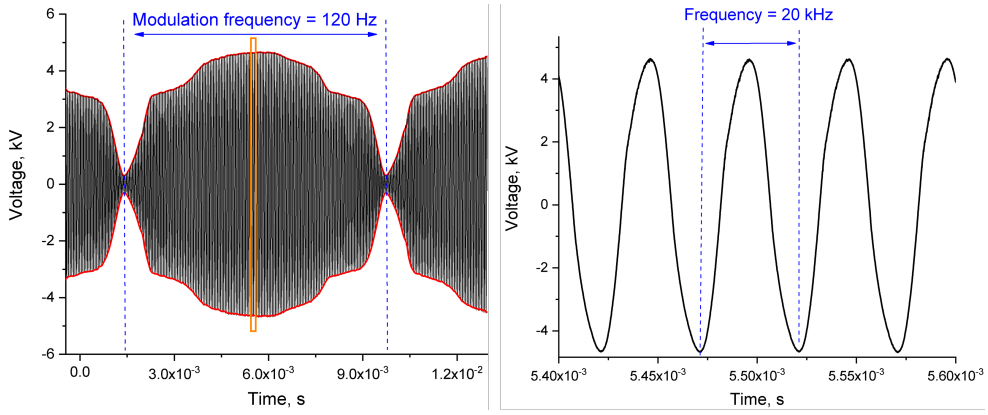

Fig. S3. Experimental measurements of the voltage profile of the sDBD. The sinusoidal waveform has a frequency of 20 kHz (right) while the modulation of the waveform has a frequency of 120 Hz (left). The peak voltage varies from 0.3 kV to 5 kV

The instantaneous charge Q is measured by

$$Q = C_{probe} \cdot \Delta V_{probe} \tag{S1}$$

The energy consumed by the dielectric barrier discharge in a voltage cycle is obtained by averaging the product $Q \cdot \Delta V$ over a whole period T, which is given by N points separated by the time interval Δt:

$$E = \frac{1}{N} \Sigma_{i=1}^{N} Q \cdot \Delta V \tag{S2}$$

Once E is obtained, the dissipated power is given by $P = E/T$ as

$$T = \frac{1}{N^2 \Delta t} \Sigma_{i=1}^{N} Q \cdot \Delta V \tag{S3}$$

The Lissajous plots with different peak voltages are shown in Fig. S4, with the instantaneous power calculated based on the Eqn. S3. When the imposed electric field is small, the Lissajous plot is closer to a straight line. If the voltage amplitude is high enough for the plasma ignition, during the two phases of plasma activity the Lissajous plot opens up and forms a closed curve figure.

One can further plot the modulated peak voltage and the measured power versus time in one cycle as shown in Fig. S5. The instantaneous power follows the change in the variation of the peak voltage. For one modulation cycle, the averaged power into the plasma discharge is approximately 20-25 watts.

However, in a DBD, the electric current and the deposited power flowing into the circuit can be viewed as the superimposition of a low-frequency sinusoidal capacitive current/energy, which is almost independent of plasma presence along the surface, and a discharge current/energy, which is associated with plasma microdischarges and appears as a series of fast pulses at the

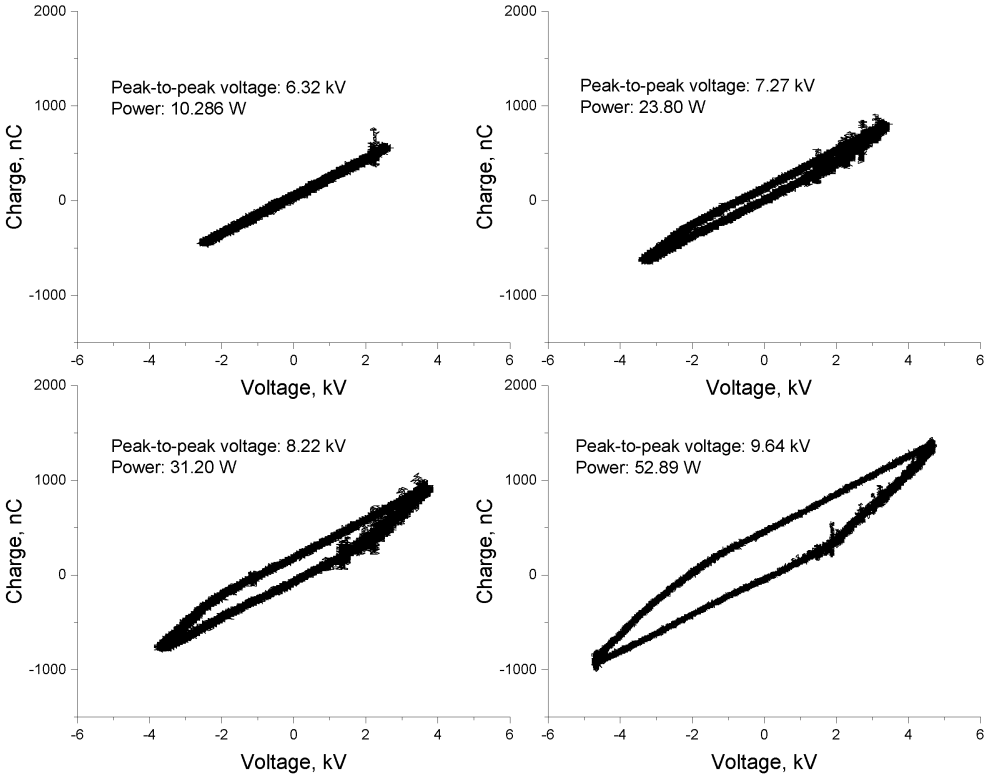

Fig. S4. Experimental measurements of the Lissajous plots at different peak-to-peak voltages, from 6.32 kV to 9.64 kV.

nanosecond time scale. From previous discussions of the heating mechanism of the sDBD [3], the energy inefficiency caused by the heating is determined by the applied voltage, dielectric material, and the geometry.

C. RGA Calibration of the CO_2 Peak (amu = 44)

By flowing a known concentration of CO_2, one can correlate RGA signals (amu = 44) with the molar fractions of CO_2 gas. In the calibration experiment, a 5% CO_2 cylinder (bath: O_2) is mixed with a O_2 cylinder. By varying the flow rates of these two sources, we calibrate the RGA signals (unit: Torr) with molar concentrations, as shown in Fig. S6. The peak CO_2 RGA signals are in the range of $6 \times 10^{-8} - 1.0 \times 10^{-7}$, which correspond to the molar fraction of 2% - 4%.

D. Optical Diagnostics: UV-Vis Absorption Spectroscopy

The concentrations of the O_3, NO, NO_2, NO_3, N_2O_4, and N_2O_5 were calculated by using the optical absorption spectroscopy. Table S1 shows the literature data in which the absorption cross-section data were collected. The averaged cross-section data from 220 nm to 550 nm (in Fig. S7) were used to convert the absorption spectra to gas concentrations. It should be noted that in our experimental setup, N_2O_3 was not a measurable species due to its limited available absorption cross-section data, which did not align with our target wavelengths. Other species such as H_2O, CO_2, N_2O, and O_2 were also possible to be in the product, but they were also excluded from the calculation because of their small cross-sections (H_2O of $10^{-25\sim26}$, CO_2 of 10^{-25}, N_2O of 10^{-24}, and O_2 of 10^{-26} [cm^2/molecule]) at our target wavelengths. The absorbance was determined by the Beer-Lambert law as

$$A(\lambda) = -ln(\frac{I(\lambda)}{I_0(\lambda)}) = \Sigma_{i=1}^{n} n_i \sigma_i(\lambda) d \tag{S4}$$

where A is the absorbance, I is the transmitted light intensity, I_0 is the light intensity before entering the chamber, n_i is the concentration of i^{th} species, and σ_i is the absorption cross-section of i^{th} species. The absorption path length is d, which was determined as 33 cm.

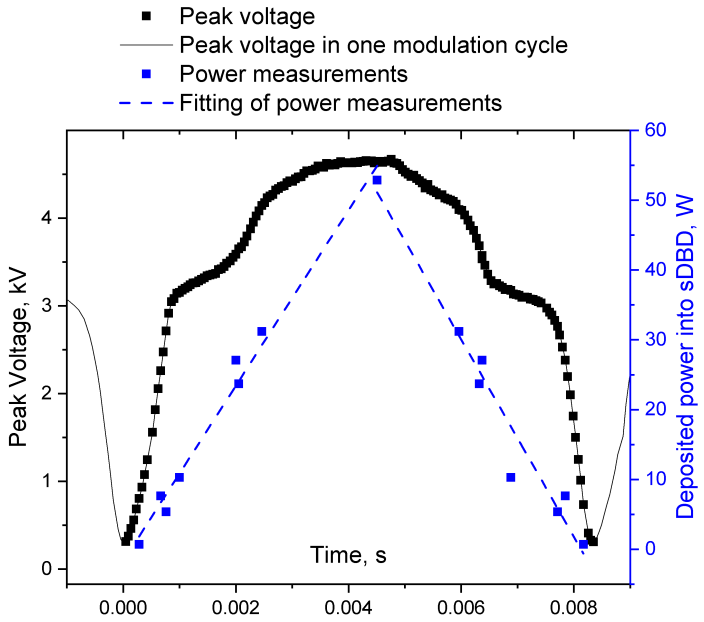

Fig. S5. The modulated peak voltage and the measured power versus time in one modulation cycle.

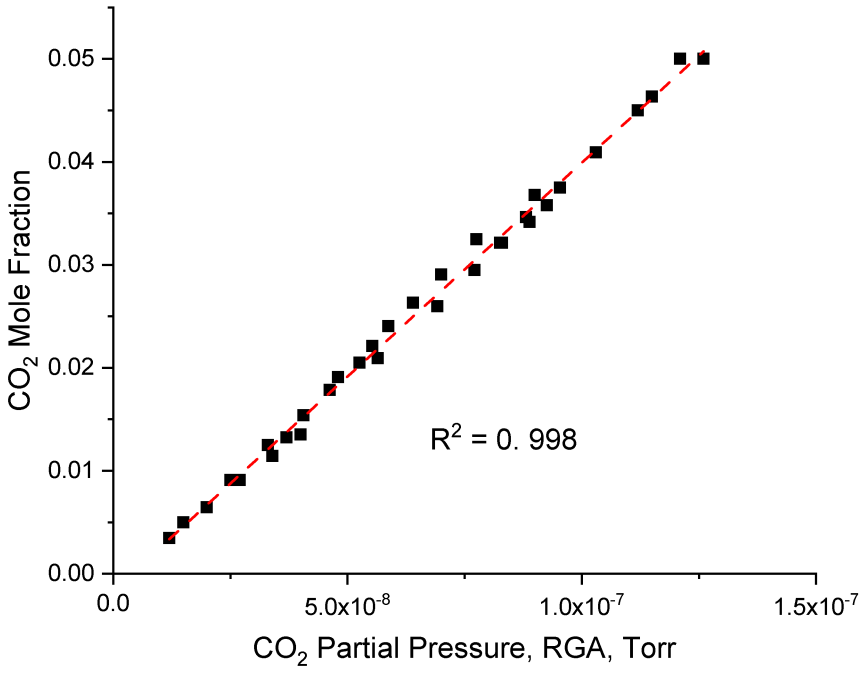

Fig. S6. Calibration at amu = 44: CO_2 RGA ion gauge pressure versus the known CO_2 mole fraction.

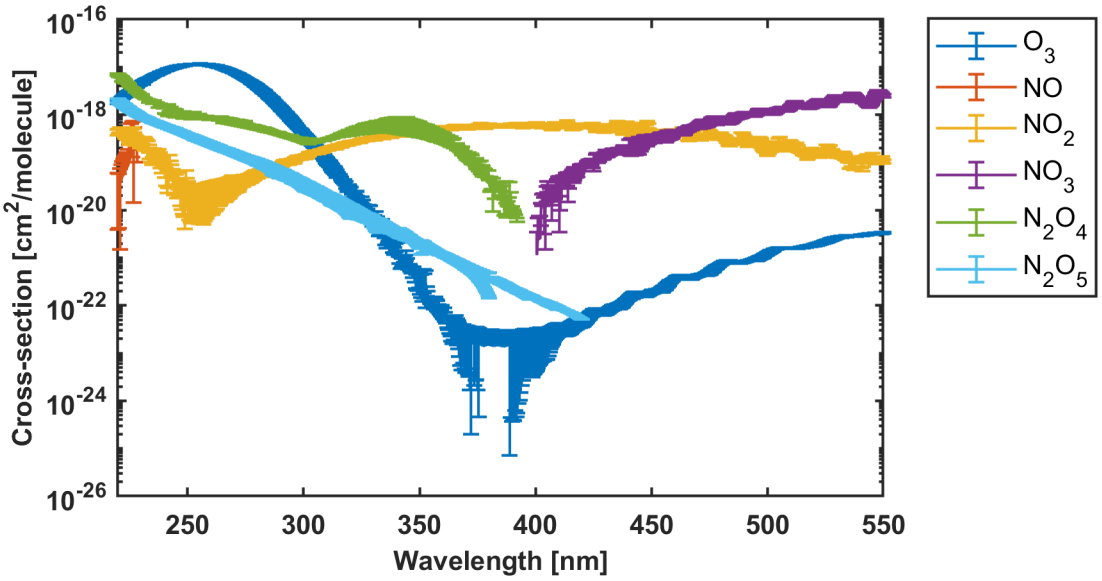

Fig. S7. The absorption cross-section of O_3, NO, NO_2, NO_3, N_2O_4, and N_2O_5 in the wavelength range of 220 nm $\sim$ 550 nm. The error bars indicate the standard deviation of the cross-section from different references.

Species	Refs
O_3	[4–22]
NO	[23, 24]
NO_2	[7, 15, 25–34]
NO_3	[15, 28, 30, 35–40]
N_2O_4	[25, 27, 33, 41]
N_2O_5	[15, 28, 30, 42–46]

Table S1. The references of absorption cross-section data for O_3 and NO_x species.

The background noise was captured when the lamp was turned off. The noise was removed before the numerical fitting. The gas concentration was calculated only when the signal-to-noise ratio was greater than two at 250 nm. The iteration fitting was implemented by the MATLAB function "fminsearch" to find the best fit between experimental absorbance and simulated absorbance. The wavelength range was divided into four regions, which were 425 nm $\sim$ 550 nm, 330 nm $\sim$ 385 nm, 232 nm $\sim$ 305 nm, and 220 nm $\sim$ 230 nm. This division is to reduce the number of unknowns in each iteration, hence only species with relatively high cross-sections in each region were calculated. At the first region of 425 nm $\sim$ 550 nm, the concentrations of NO_3 and NO_2 were calculated with the initial guesses. The second region of 330 nm $\sim$ 385 nm was for determining the N_2O_4 concentration with the known NO_3 and NO_2 concentrations. The third region of 232 nm $\sim$ 305 nm was used to determine the concentrations of O_3 and N_2O_5. The NO concentration was determined at the fourth region of 220 nm $\sim$ 230 nm. After four calculations, one iteration was performed at the whole wavelength range of 220 nm $\sim$ 550 nm.

E. Estimation of the Energy Consumption

For the experiments conducted in air, the corresponding CO_2 regeneration efficiency, η, defined as:

$$\eta = \frac{\text{Deposited power into the plasma}}{\text{Generated } CO_2 \text{ flow rate}} \quad [\text{kWh/tCO}_2]$$

The deposited power varies with time (as shown in Fig. S5). The average power injected into the plasma plate is estimated to be 20 watts. Further taking the overlap area of the plasma discharge and the aluminium tray into account, the averaged plasma power deposited for CO_2 regeneration is $\sim$ 8 w.

Considering the heat loss of the plasma plate, similarly as estimated in previous literature [3], we estimate the heat loss is $\Delta Q = h(T - T_\infty)A$, where $h \approx 10\ W/m^2K$, $A = 60\ cm^2 = 6 \times 10^{-3}\ cm^2$, $(T - T_\infty)$ is $\approx 100 - 150K$ (T: temperature of the plasma plate, T_∞: temperautre of the free stream air). As a result, the heat loss is 6-9 w. Therefore, the order of magnitude estimate for the energy in activating chemicals is $\sim$ 1w.

2. ZERO-DIMENSIONAL CHEMICAL KINETIC MODEL

Plasma-assisted carbonate regeneration has vast time scale differences, from nanoseconds to hours. Our experimental configuration also has vast spatial scale differences, from the sheath length in micrometres, to the reactor length in centimetres. Therefore, it is unrealistic to replicate the exact experimental results. The objective of the chemical kinetic model is to identify the dominant kinetic mechanism and predict the observed chemical dynamics qualitatively.

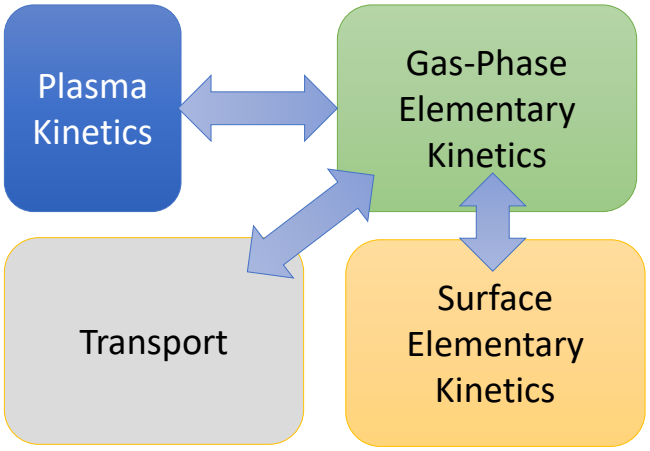

Fig. S8. The modeling consists of four parts, including plasma kinetics, gas-phase elementary kinetics, transport, and surface kinetics.

A. Plasma kinetics

In air plasma kinetics literature [47], NO is believed to be the major quencher of O_3: NO reacts with O_3 to generate NO_2 and O_2. NO_2 further quenches O_3 and is converted into NO_3. However,

during the O_3 to NO_x mode transition reported in this work, the temperature increase in the vicinity of the electrode is minimal, less than $\sim 50^{\circ}C$ from room temperature. Therefore, the NO generation is not due to the thermal mechanism [48], in which the reaction between N atoms and O_2/O_3 dominate. The alternative channel is the reaction between vibrationally excited nitrogen molecules (N_2(v)) and O atoms. As the discharge power increases, the fraction of vibrationally excited nitrogen increases, thereby greatly increasing the rate of creation of NO.

The detailed modelling of air plasma kinetics, coupling tens of species and hundreds of reactions, has been reported previously [49]. Due to the minute-long time scale of the problem, it is intractable to resolve electron energy evolution and simulate plasma kinetics in a detailed fashion. Instead, three global parameters (summarized in Table. S2) are fitted to characterize the electron-impact plasma kinetics.

Index	Reaction	Global Parameter	Fitting Ranges
E-1	e + O_2 $\longrightarrow$ e + O + O	n_O	1.0×10^{10} - 1.0×10^{12} cm^{-3}
E-2	e + N_2 $\longrightarrow$ e + N_2(v)	T_v^0	5,000 - 8,000 K
		τ_v	500 - 5500 s

Table S2. A list of electron-impact reactions and fitting parameters.

Three fitting parameters include the atomic oxygen number density (n_O), the vibrational temperature at steady state (T_v^0), and the time scale of the vibrational temperature increase (τ_v). These fitting parameters are determined to reproduce the measured profiles of ozone and NO_x density, from the UVAS measurements. The fitted n_O values are reasonable and consistent with previous measurements in similar discharges [50]. The long time scale of fitted τ_v may be caused by the collisional radiation by excitation and de-excitation in the air plasma discharge.

$$n_{N_2(v)} = n_{N_2} F_{v>12} = n_{N_2} exp(-\frac{12\Delta\epsilon_V}{k_b T_v}) \quad \text{(S5)}$$

$$T_v = T_g + T_v^0(1 - exp(-t/\tau_v)) \quad \text{(S6)}$$

$\Delta\epsilon_V$ (= 0.29 eV) is the vibrational energy for harmonic oscillators. k_b is the Boltzmann constant and T_g(= 300K) is the gas temperature. In Eqn (S5), vibrationally excited nitrogen at levels above v = 12 contributes to the non-equilibrium NO generation. The vibrational energy distribution function (VEDF) is approximated by Maxwell distribution for simplicity.

B. Gas-phase elementary kinetics and transport

For gas-phase kinetics, we developed a simple, parameterized model with reactions listed in S4 to describe the gas-phase kinetics. The focus is the evolution of the number density of key species such as O_3, NO, and CO_2 in a well-mixed control volume without the spatial gradient.

The loss caused by diffusion and convection is considered in the model by adding the extra loss term with τ_{dif} = 40 - 200 s. It is obtained by measuring the decay rate of NO_x density after plasma discharge is turned off.

The equations were solved using an ordinary differential equation solver using ZDPlaskin. Fig. S9 shows a comparison between the measured profile and the model output without the presence of calcium carbonate powders. The fitted parameters are $n_O = 1.4 \times 10^{11} m^{-3}$, $T_v^0 = 7500K$, and $\tau_v = 1.2 \times 10^3 s$. These parameters were uniquely determined to reproduce the measured ozone density: n_O and T_v^0 decide the slope of the rising rate and decay rate of ozone density. The cross-over time was determined by τ_v. In this case, the cross-over time, the initial O_3 number density, steady-state NO and NO_2 number density are reasonably well-predicted. Different increasing/decreasing trend for O_3 and NO_x is attributed to the simplified kinetic scheme.

C. Surface kinetics

We further include a simplified and hypothesized surface kinetic mechanism involving atomic oxygen, surface calcium species (CaO_2^*, CaO, $CaCO_3$), and surface NO_x species to explain the CO_2 formation in the presence of $CaCO_3$ powders and plasmas. Here calcium peroxide [55] is

Index	Reaction	Rate constant	Refs
G-1	$O + O_2 + M \longrightarrow O_3 + M$	3.4×10^{-34}	[51]
G-2	$O + NO + M \longrightarrow NO_2 + M$	1.0×10^{-31}	[52]
G-3	$O + N_2(v) \longrightarrow NO + N$	1.0×10^{-11}	[53]
G-4	$O_3 + NO \longrightarrow NO_2 + O_2$	1.8×10^{-14}	[54]
G-5	$O_3 + NO_2 \longrightarrow NO_3 + O_2$	3.4×10^{-17}	[52]
G-6	$O_3 + M \longrightarrow O + O_2 + M$	1.23×10^{-26}	[52]

Table S3. A list of reactions and the rate constants in the gas phase. The unit of the rate constant is cm^3/s for two-body reactions and cm^6/s for three-body reactions. The temperature dependence is neglected as the experiment is performed at room temperature. M denotes the third body.

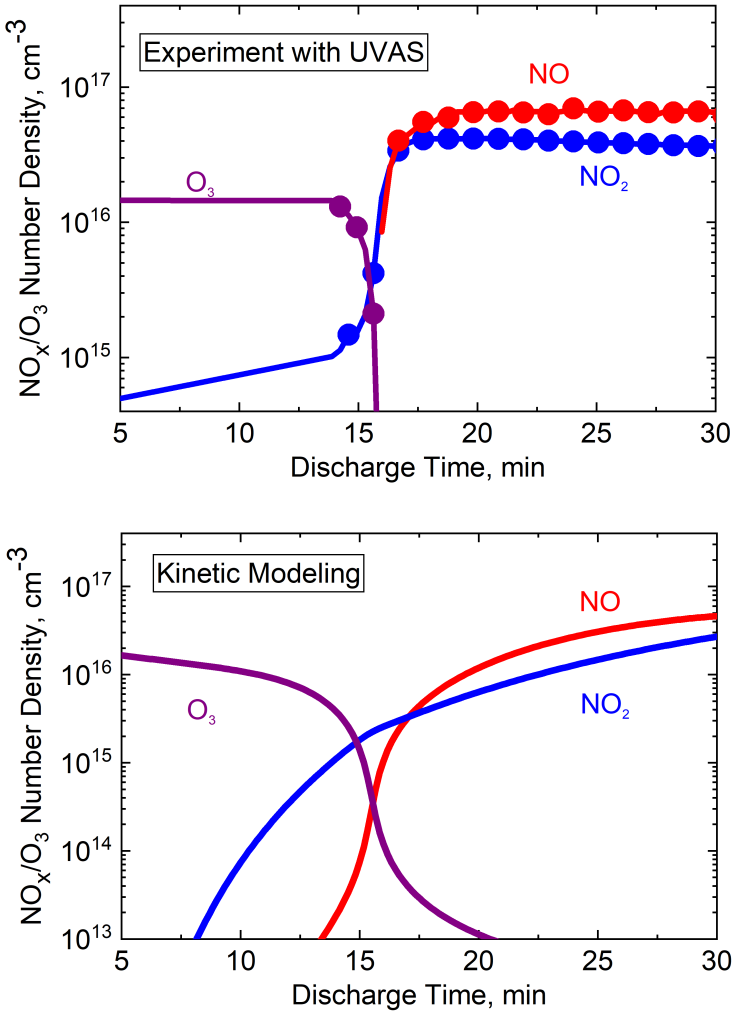

Fig. S9. A comparison between experimental measurements and kinetic modelling for the case without $CaCO_3$ powders. Fitting parameters: $n_O = 1.4 \times 10^{11}$ cm^{-3}. $T_v^0 = 7500$ K. $\tau_v = 1.2 \times 10^3$s.

a hypothesized intermediate species. The model output is also provided as shown in Fig. S10. The simplified model can predict the CO_2 formation and the cross-over time. However, the NOx formation differs from the experiment measurements by almost one order of magnitude. From this simplified kinetic scheme, with the presence of calcium carbonates, the oxygen atom gets adsorbed by the carbonate surface, which delays the vibrational quenching reaction (G-3) to form NO. NO is a key intermediate for O_3 consumption (G-4) and the NO_x-O_3 mode transition. So with less available oxygen atoms in the gas phase, NO formation is inhibited and the NO_x-O_3 mode transition is delayed with the presence of the calcium carbonates. Oxygen atoms are adsorbed to the surface to form CaO_2^* to release CO_2. Future careful modelling for this problem is still needed.

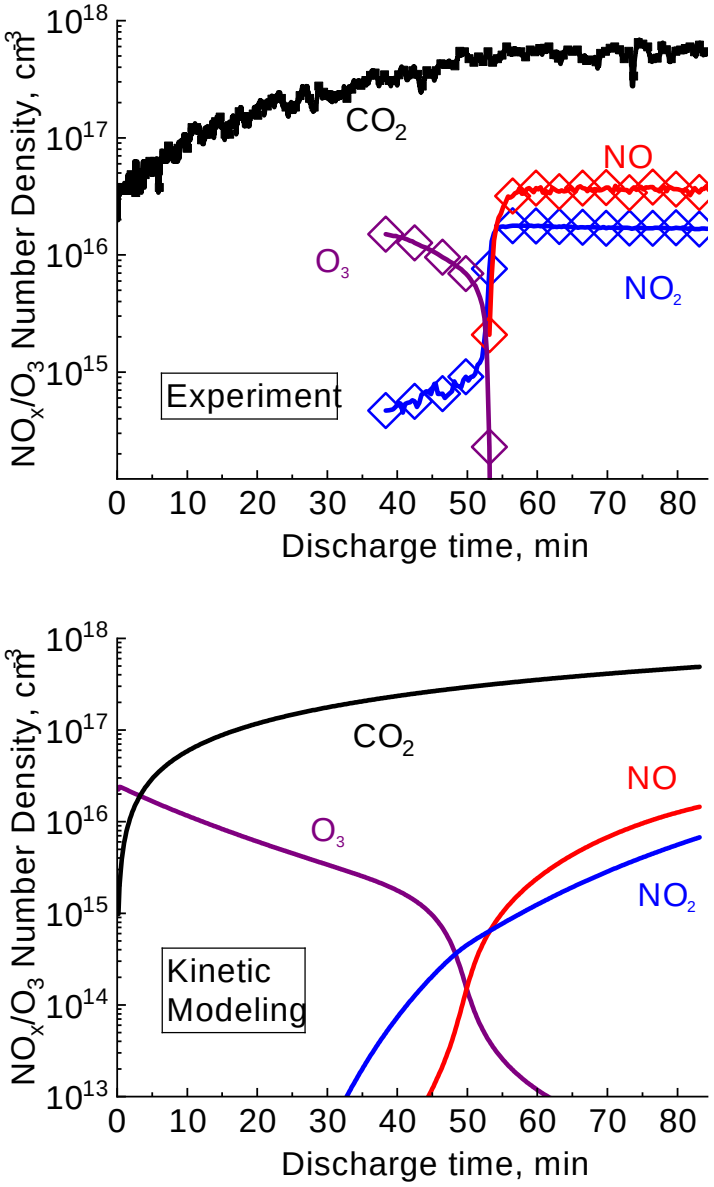

Fig. S10. A comparison between experimental measurements and kinetic modeling for the case with $CaCO_3$ powders. Fitting parameters: $n_O = 1.4 \times 10^{11}$ cm^{-3}. $T_v^0 = 7500$ K. $\tau_v = 5.0 \times 10^3$s.

Index	Reaction	Rate constant	Refs
S-1	$O(g) + CaCO_3(s) \longrightarrow CaO_2^*(s) + CO_2(g)$	1.0×10^{-12}	[56]
S-2	$CaO_2^*(s) + O(g) \longrightarrow CaO(s) + O_2(g)$	2.2×10^{-11}	[56]
S-3	$H_2O(g) + NO_2(g) + NO_2(g) \longrightarrow HONO(g) + HNO_3(g)$	7.9×10^{-39}	[57]
S-4	$CaCO_3(s) + 2\,HNO_3(g) \longrightarrow Ca(NO_3)_2(s) + H_2O(g) + CO_2(g)$	1.0×10^{-39}	estimated

Table S4. A list of proposed surface reactions. The unit of the rate constant is cm^3/s for two-body reactions and cm^6/s for three-body reactions. M denotes the third body. $CaCO_3$ number density is estimated, which is determined by the surface density of $CaCO_3$ powders.

3. SUPPLEMENTARY MEASUREMENTS

A. Air Plasma Treatment of Calcium Carbonate and Sodium Carbonate

The non-equilibrium regeneration is sensitive to the sorbent material. Changing $CaCO_3$ to Na_2CO_3 results in a noticeable decrease in the CO_2 yield. This indicates that engineered sorbent materials for non-equilibrium regeneration are needed to optimize energy efficiency.

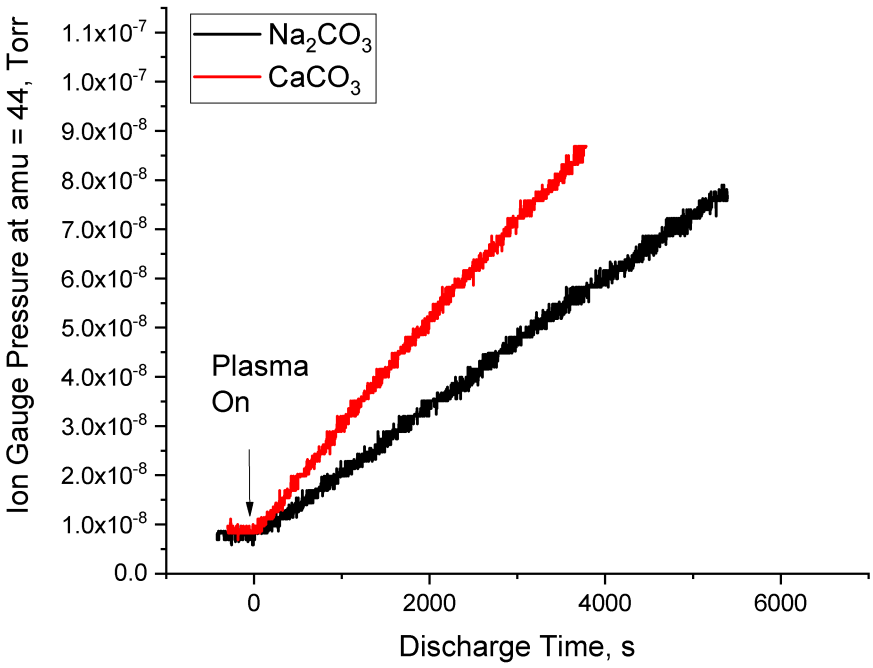

Fig. S11. Under the same air plasma treatment, Na_2CO_3 is less efficient for generating CO_2, compared with $CaCO_3$.

B. Comparison between flowing a NO_x mixture through the $CaCO_3$ powder and plasma-based carbonate regeneration

To verify the effect of non-equilibrium plasma, a known concentration of NO (2%, balanced by N_2) is flowing into the reactor with plasma off. RGA shows that CO_2 concentration is not increased with the presence of a high concentration of NO_x species. Similarly, when a mixture of NO/O_2 is flowing into the reactor, the CO_2 increase is even minor. These measurements demonstrate that

the non-equilibrium surface process is the key to the CO_2 desorption.

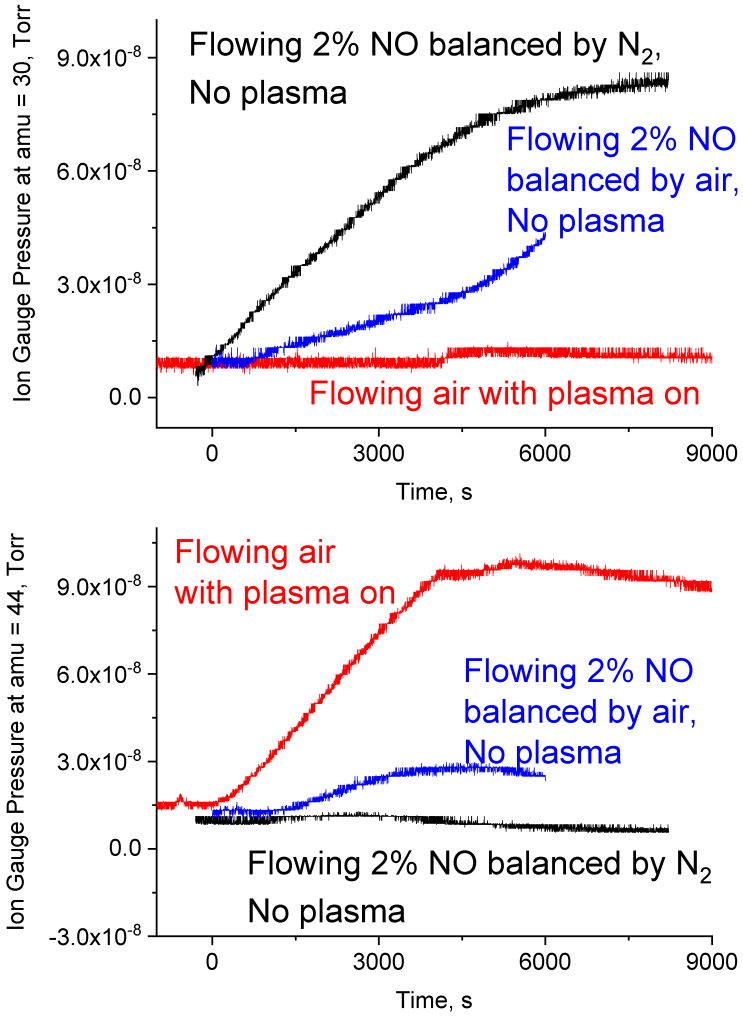

Fig. S12. Comparison of RGA signals at amu = 30 and 44 for three cases: 1) flowing air with plasma on; 2) flowing 2% NO with plasma off; 3) flowing 2% NO with O_2 with plasma off

C. Argon and Oxygen Plasma Treatment of Calcium Carbonate Powders

Suitable gases are critical for the regeneration efficiency. Argon plasma is completely inert to the CO_2 generation. Oxygen plasma can generate CO_2 but is less efficient compared to air plasma. Future work includes the regeneration experiment of sorbent materials using more reactive plasmas such as H_2 and CH_4.

D. Comparison of Non-Equilibrium and Equilibrium Carbonate Decomposition

As shown in Fig. S14, the equilibrium pressure of $CaCO_3$ is over tens of orders of magnitude larger at 350 K under the plasma operation. In other words, the effects of plasma are non-thermal: instead of heating the carbonate powder to a higher temperature, it goes through chemical conversions to release CO_2.

E. Ratio between areas under different peaks for XPS Diagnostics

We integrate the area under different peaks, *i.e.*, Ca, C and O peaks, and calculate the ratio between different peaks as shown in Table. S5. This is used to qualitatively determine the change in composition in the solid phase.

From Table. S5, after the plasma processing, the ratio of C/Ca drops compared to that in the control group. It means that carbon is released from the powder. For the O peak, the ratio goes

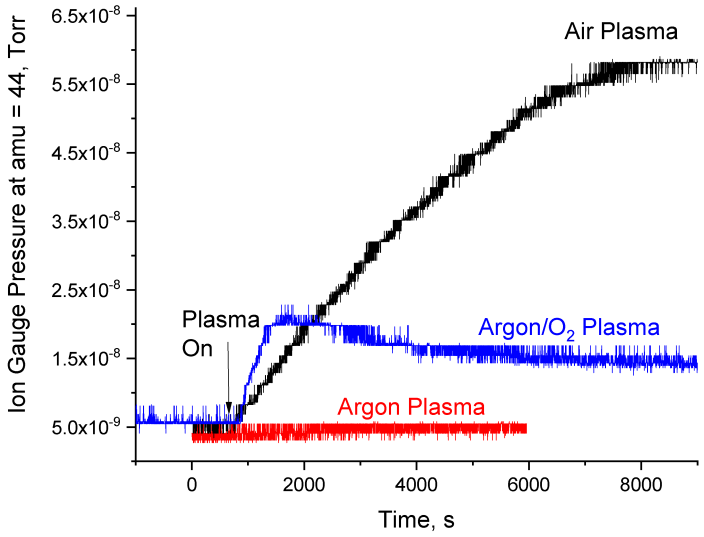

Fig. S13. The comparison of RGA CO_2 signals under argon, 50% oxygen (balanced by Ar) and air plasmas.

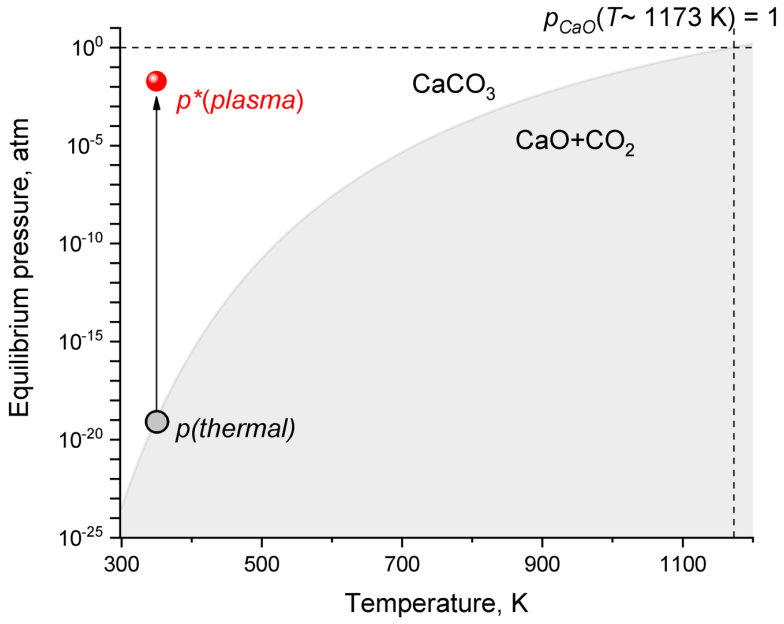

Fig. S14. Equilibrium pressure of $CaCO_3$ relative to temperature [58]. The red dot indicates the data point in the plasma case.

Case	C/Ca	O/Ca
Base case (without plasma treatment)	0.18	1.6
Case with air plasma treatment	0.16	1.8
Case with oxygen plasma treatment	0.14	1.9

Table S5. Ratio of areas under different peaks from XPS diagnostics. The carbon peak is at ∼286.4 eV. Another carbon peak is the adventitious carbon (∼282 eV). The calcium twin peaks are at 343.9 eV and 347.4 eV. The oxygen peak is at ∼528.8 eV.

up as the oxygen peaks are broadened, as shown in Fig.4 in the main context. The above analysis provides evidence for the proposed non-equilibrium regeneration mechanism: CO_2 is released from the carbonate powder by reactive air plasmas.

F. Reproducibility of Measurements

We repeated the experiments through the summer of 2023. For RGA signals, changes in the NO and O_2 signals are reproducible and significant. We provide additional experiments measured on different dates under the same conditions shown in Figs. S15 and S16 to show the experimental consistency.

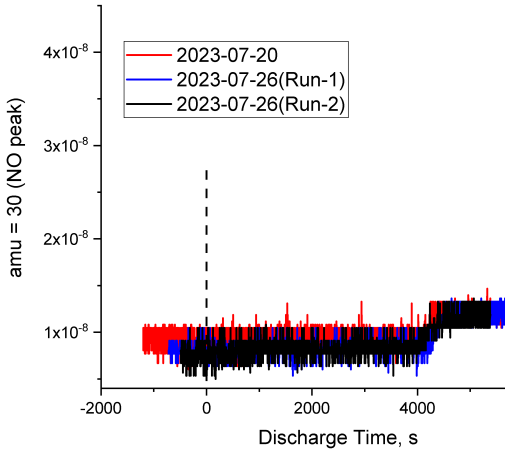

Fig. S15. Repeated RGA measurements at amu = 30 on different runs with same experimental conditions.

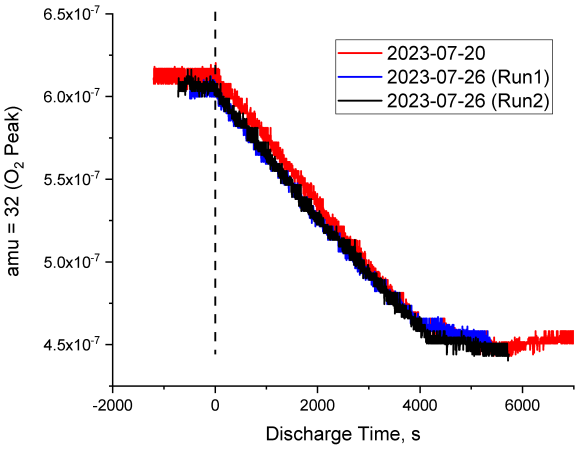

Fig. S16. Repeated RGA measurements at amu = 32 on different runs with same experimental conditions.

In addition, we also conducted RGA measurements under different but similar conditions, for example, with different powder loadings (Fig. S17), with different flow residence times (Fig. S18), etc. These additional experiments were designed to verify the robustness of the observed CO_2 desorption phenomena and to ascertain the reproducibility of the results across a wider range of operational parameters. In all of those controlled experiments, we observed consistent patterns that confirmed our findings. Variations in flow residence time and powder loading did not significantly alter the concentration profiles of the measured species, suggesting that the underlying mechanisms remain stable across these parameters.

We didn't provide those measurements in the main context because the objective of this paper is to reveal a novel mechanism for CO_2 desorption, not to optimize the reaction conditions. Future studies should focus on the parametric and quantitative studies.

For UVAS diagnostics, we conducted experiments repeatedly from 2023-08-15 to 2023-08-18 for various flow conditions. The cross-overs of O_3 and NO or NO_2 are clearly and consistently observed. Here we provide two representative cases conducted on different days with the same

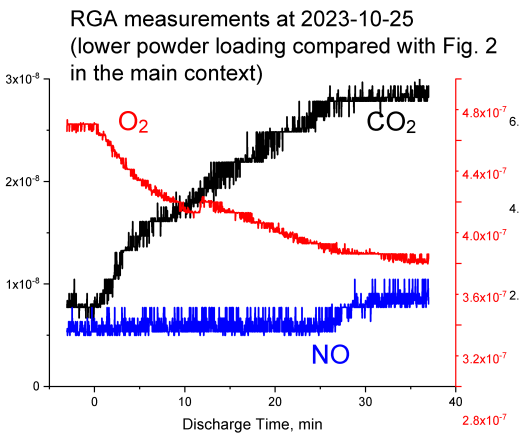

Fig. S17. RGA measurements at amu = 30, 44 and 32 with a lower $CaCO_3$ powder loading.

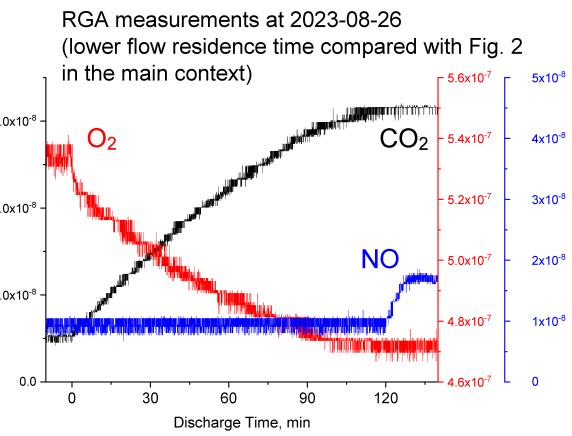

Fig. S18. RGA measurements at amu = 30, 44 and 32 with a lower flow residence time.

flow conditions (air flowing through $CaCO_3$ powders), shown in Fig. S19. Note the flow rate is 50 sccm in those two cases. As a result, the transition time is delayed compared to the result in the main context (10 sccm flow rate).

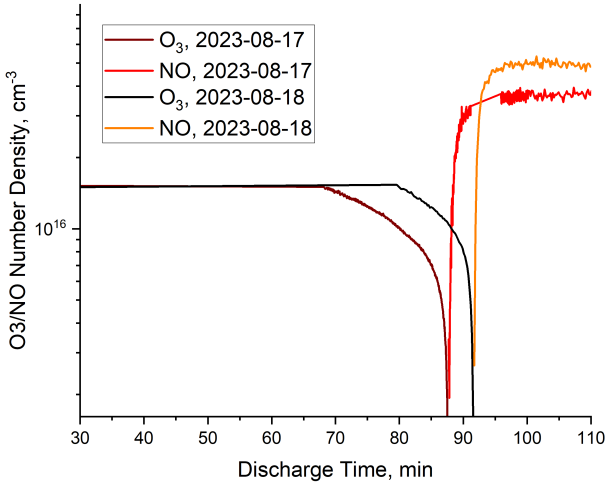

Fig. S19. Representative repeated UVAS measurements for the same flow conditions.

We conducted three series of XPS measurements under different controlled conditions. For similar experiment inputs, the results are consistent and reproducible. We provide representative N1s spectra as an example, as shown in Fig. S20.

In conclusion, the consistency of the data across varying experimental conditions reinforces the reliability of our findings.

G. Effects of Distance

The authors performed a series of experiments to understand the effects of distance. As provided in Fig. S21, when the powder is placed under discharge, the distance between the plasma and the powder will not significantly influence the results. However, if the powder is moved out of the plasma zone but still within the reactor, the CO_2 desorption will decrease dramatically. Clearly, in the plasma zone, the CO_2 desorption is reaction-controlled, while moving out of the plasma zone, it is more diffusion-controlled.

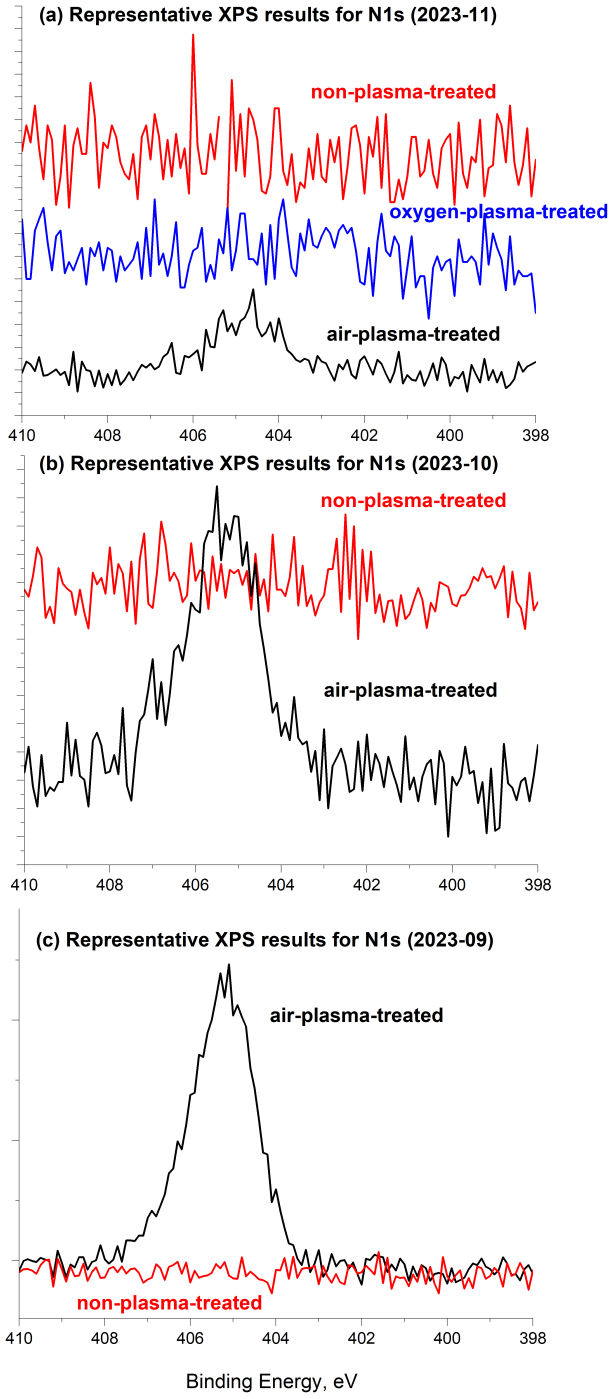

Fig. S20. Representative repeated XPS measurements for N1s peak.

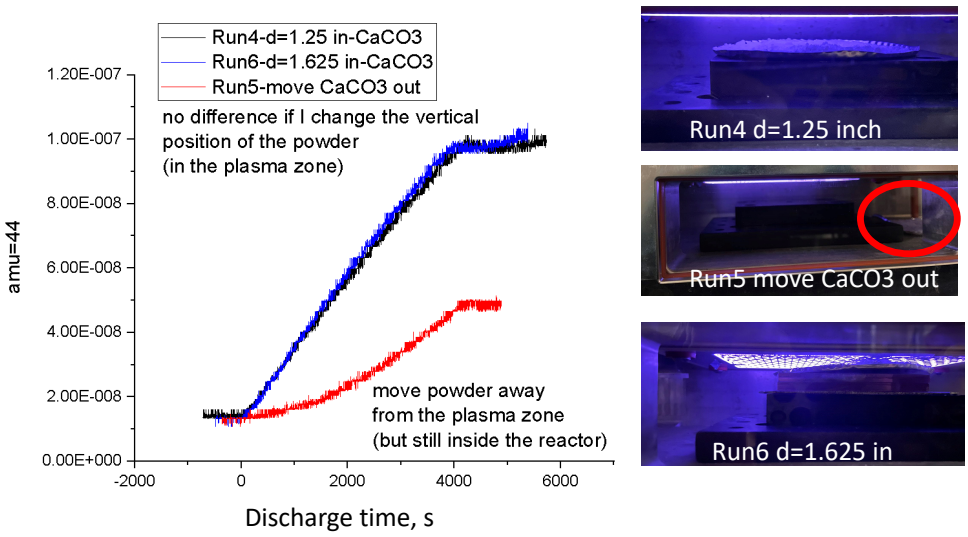

Fig. S21. Supplementary information for varying gap distance d in the chamber.

As the objective of the paper is to propose a new non-equilibrium chemical mechanism, we did not provide a detailed parametric discussion of the effect of distance on CO_2 desorption.

REFERENCES

1. R. Wang, Y. Yang, S. Chen, H. Jiang, and P. Martin, "Power calculation of pulse power-driven dbd plasma," IEEE Transactions on Plasma Sci. **49**, 2210–2216 (2021).
2. I. Biganzoli, R. Barni, A. Gurioli, R. Pertile, and C. Riccardi, "Experimental investigation of lissajous figure shapes in planar and surface dielectric barrier discharges," in *Journal of Physics: Conference Series*, vol. 550 (IOP Publishing, 2014), p. 012039.
3. F. Rodrigues, J. Pascoa, and M. Trancossi, "Heat generation mechanisms of DBD plasma actuators," Exp. thermal fluid science **90**, 55–65 (2018).
4. M. Ackerman, "Ultraviolet solar radiation related to mesospheric processes," in *Mesospheric models and related experiments: proceedings of the fourth esrin-eslab symposium held in Frascati, Italy, 6–10 July, 1970*, (Springer, 1971), pp. 149–159.
5. D. Astholz, A. Croce, and J. Troe, "Temperature dependence of the ozone absorption coefficient in the hartley continuum," The J. Phys. Chem. **86**, 696–699 (1982).
6. K. Becker, U. Schurath, and H. Seitz, "Ozone–olefin reactions in the gas phase 1. rate constants and activation energies," Int. J. Chem. Kinetics **6**, 725–739 (1974).
7. K. Bogumil, J. Orphal, T. Homann, S. Voigt, P. Spietz, O. Fleischmann, A. Vogel, M. Hartmann, H. Kromminga, H. Bovensmann *et al.*, "Measurements of molecular absorption spectra with the sciamachy pre-flight model: instrument characterization and reference data for atmospheric remote-sensing in the 230–2380 nm region," J. Photochem. Photobiol. A: Chem. **157**, 167–184 (2003).
8. J. Brion, A. Chakir, D. Daumont, J. Malicet, and C. Parisse, "High-resolution laboratory absorption cross section of O_3. temperature effect," Chem. physics letters **213**, 610–612 (1993).
9. J. Brion, A. Chakir, J. Charbonnier, D. Daumont, C. Parisse, and J. Malicet, "Absorption spectra measurements for the ozone molecule in the 350–830 nm region," J. atmospheric chemistry **30**, 291–299 (1998).
10. J. B. Burkholder, J. J. Orlando, and C. J. Howard, "Ultraviolet absorption cross sections of chlorine oxide (cl2o2) between 210 and 410 nm," J. Phys. Chem. **94**, 687–695 (1990).
11. J. P. Burrows, A. Richter, A. Dehn, B. Deters, S. Himmelmann, S. Voigt, and J. Orphal, "Atmospheric remote-sensing reference data from gome—2. temperature-dependent absorption cross sections of o3 in the 231–794 nm range," J. quantitative spectroscopy radiative transfer **61**, 509–517 (1999).
12. W. B. DeMore and O. Raper, "Hartley band extinction coefficients of ozone in the gas phase and in liquid nitrogen, carbon monoxide, and argon," The J. Phys. Chem. **68**, 412–414 (1964).
13. M. Griggs, "Absorption coefficients of ozone in the ultraviolet and visible regions," The J. Chem. Phys. **49**, 857–859 (1968).
14. E. C. Inn and Y. TANAKA, "Ozone absorption coefficients in the visible and ultraviolet regions," (ACS Publications, 1959).
15. S. Sander, R. Friedl, D. Golden, M. Kurylo, G. Moortgat, P. Wine, A. Ravishankara, C. Kolb, M. Molina, B. Finlayson-Pitts *et al.*, "Chemical kinetics and photochemical data for use in atmospheric studies evaluation number 15," Tech. rep. (2006).
16. N. Mason, J. Gingell, J. Davies, H. Zhao, I. Walker, and M. Siggel, "Vuv optical absorption and electron energy-loss spectroscopy of ozone," J. Phys. B: At. Mol. Opt. Phys. **29**, 3075 (1996).
17. L. Molina and M. Molina, "Absolute absorption cross sections of ozone in the 185-to 350-nm wavelength range," J. Geophys. Res. Atmospheres **91**, 14501–14508 (1986).
18. N. Tsi-Ze and C. S. Piaw, "L'absorption da la lumiere par l'ozone entre 3050 et 3400 a," Compt. Rand. Acad. Sci. Paris **195**, 309–311 (1932).
19. A. Serdyuchenko, V. Gorshelev, M. Weber, W. Chehade, and J. P. Burrows, "High spectral resolution ozone absorption cross-sections–part 2: Temperature dependence," Atmospheric Meas. Tech. **7**, 625–636 (2014).
20. J. W. Simons, R. J. Paur, H. A. Webster III, and E. J. Bair, "Ozone ultraviolet photolysis. vi. the ultraviolet spectrum," The J. Chem. Phys. **59**, 1203–1208 (1973).
21. M. Trolier, R. Mauldin, and A. Ravishankara, "Rate coefficient for the termolecular channel of the self-reaction of chlorine monoxide," J. Phys. Chem. **94**, 4896–4907 (1990).
22. S. Voigt, J. Orphal, K. Bogumil, and J. Burrows, "The temperature dependence (203–293 k) of the absorption cross sections of o3 in the 230–850 nm region measured by fourier-transform spectroscopy," J. Photochem. Photobiol. A: Chem. **143**, 1–9 (2001).
23. W. Chang, G. Cooper, and C. Brion, "Absolute optical oscillator strengths for the photoabsorption of nitric oxide (5–30 ev) at high resolution," Chem. physics **170**, 111–121 (1993).

24. B. Thompson, P. Harteck, and R. Reeves Jr, "Ultraviolet absorption coefficients of co2, co, o2, h2o, n2o, nh3, no, so2, and ch4 between 1850 and 4000 a," J. Geophys. Res. **68**, 6431–6436 (1963).
25. A. M. Bass, A. E. Ledford Jr, and A. H. Laufer, "Extinction coefficients of no2 and n2o4," J. Res. Natl. Bureau Standards. Sect. A, Phys. Chem. **80**, 143 (1976).
26. J. Burrows, A. Dehn, B. Deters, S. Himmelmann, A. Richter, S. Voigt, and J. Orphal, "Atmospheric remote-sensing reference data from gome: Part 1. temperature-dependent absorption cross-sections of no2 in the 231–794 nm range," J. Quant. Spectrosc. Radiat. Transf. **60**, 1025–1031 (1998).
27. T. Hall Jr and F. Blacet, "Separation of the absorption spectra of no2 and n2o4 in the range of 2400–5000a," The J. Chem. Phys. **20**, 1745–1749 (1952).
28. R. Atkinson, D. Baulch, R. A. Cox, J. Crowley, R. Hampson, R. Hynes, M. Jenkin, M. Rossi, and J. Troe, "Evaluated kinetic and photochemical data for atmospheric chemistry: Volume i-gas phase reactions of o x, ho x, no x and so x species," Atmospheric chemistry physics **4**, 1461–1738 (2004).
29. A. Jenouvrier, B. Coquart, and M. Merienne, "The no 2 absorption spectrum. iii: The 200–300 nm region at ambient temperature," J. atmospheric chemistry **25**, 21–32 (1996).
30. H. Johnston and R. Graham, "Photochemistry of no/sub x/and hno/sub x/compounds," Can. J. Chem.;(Canada) **52** (1974).
31. M. Merienne, A. Jenouvrier, and B. Coquart, "The no 2 absorption spectrum. i: Absorption cross-sections at ambient temperature in the 300–500 nm region," J. Atmospheric Chem. **20**, 281–297 (1995).
32. T. Nakayama, M. Y. Kitamura, and K. Watanabe, "Ionization potential and absorption coefficients of nitrogen dioxide," The J. Chem. Phys. **30**, 1180–1186 (1959).
33. W. Schneider, G. K. Moortgat, G. S. Tyndall, and J. P. Burrows, "Absorption cross-sections of no2 in the uv and visible region (200–700 nm) at 298 k," J. photochemistry photobiology A: Chem. **40**, 195–217 (1987).
34. A. C. Vandaele, C. Hermans, P. C. Simon, M. Carleer, R. Colin, S. Fally, M.-F. Merienne, A. Jenouvrier, and B. Coquart, "Measurements of the no2 absorption cross-section from 42 000 cm- 1 to 10 000 cm- 1 (238–1000 nm) at 220 k and 294 k," J. Quant. Spectrosc. Radiat. Transf. **59**, 171–184 (1998).
35. R. A. Graham and H. S. Johnston, "The photochemistry of the nitrate radical and the kinetics of the nitrogen pentoxide-ozone system," The J. Phys. Chem. **82**, 254–268 (1978).
36. J. Orphal, C. Fellows, and P.-M. Flaud, "The visible absorption spectrum of no3 measured by high-resolution fourier transform spectroscopy," J. Geophys. Res. Atmospheres **108** (2003).
37. A. Ravishankara and P. Wine, "Absorption cross sections for no3 between 565 and 673 nm," Chem. physics letters **101**, 73–78 (1983).
38. S. Sander, "Temperature dependence of the no/sub 3/absorption spectrum," J. Phys. Chem.;(United States) **90** (1986).
39. R. P. Wayne, I. Barnes, P. Biggs, J. Burrows, C. Canosa-Mas, J. Hjorth, G. Le Bras, G. Moortgat, D. Perner, G. Poulet *et al.*, "The nitrate radical: Physics, chemistry, and the atmosphere," Atmospheric Environ. Part A. Gen. Top. **25**, 1–203 (1991).
40. R. Yokelson, J. B. Burkholder, R. Fox, R. K. Talukdar, and A. Ravishankara, "Temperature dependence of the no3 absorption spectrum," The J. Phys. Chem. **98**, 13144–13150 (1994).
41. H. H. Holmes and F. Daniels, "The photolysis of nitrogen oxides: N2o5, n2o4 and no2," J. Am. Chem. Soc. **56**, 630–637 (1934).
42. H. S. Johnston, S.-G. Chang, and G. Whitten, "Photolysis of nitric acid vapor," The J. Phys. Chem. **78**, 1–7 (1974).
43. M. H. Harwood, O. Rattigan, R. L. Jones, and R. Cox, "Temperature-dependent absorption cross sections for hno3 and n2o5," in *Optical Methods in Atmospheric Chemistry*, vol. 1715 (SPIE, 1993), pp. 113–124.
44. M. H. Harwood, J. B. Burkholder, and A. Ravishankara, "Photodissociation of brono2 and n2o5: Quantum yields for no3 production at 248, 308, and 352.5 nm," The J. Phys. Chem. A **102**, 1309–1317 (1998).
45. E. J. Jones and O. R. Wulf, "The absorption coefficient of nitrogen pentoxide in the ultraviolet and the visible absorption spectrum of no3," The J. Chem. Phys. **5**, 873–877 (1937).
46. F. Yao, I. Wilson, and H. Johnston, "Temperature-dependent ultraviolet absorption spectrum for dinitrogen pentoxide," The J. Phys. Chem. **86**, 3611–3615 (1982).
47. T. Shimizu, Y. Sakiyama, D. B. Graves, J. L. Zimmermann, and G. E. Morfill, "The dynamics of

ozone generation and mode transition in air surface micro-discharge plasma at atmospheric pressure," New J. Phys. **14**, 103028 (2012).
48. J. A. Miller and C. T. Bowman, "Mechanism and modeling of nitrogen chemistry in combustion," Prog. energy combustion science **15**, 287–338 (1989).
49. Y. Sakiyama, D. B. Graves, H.-W. Chang, T. Shimizu, and G. E. Morfill, "Plasma chemistry model of surface microdischarge in humid air and dynamics of reactive neutral species," J. Phys. D: Appl. Phys. **45**, 425201 (2012).
50. S. Park, W. Choe, and C. Jo, "Interplay among ozone and nitrogen oxides in air plasmas: Rapid change in plasma chemistry," Chem. Eng. J. **352**, 1014–1021 (2018).
51. H. Hippler, R. Rahn, and J. Troe, "Temperature and pressure dependence of ozone formation rates in the range 1–1000 bar and 90–370 k," The J. chemical physics **93**, 6560–6569 (1990).
52. R. Atkinson, D. Baulch, R. Cox, R. Hampson Jr, J. Kerr, M. Rossi, and J. Troe, "Evaluated kinetic and photochemical data for atmospheric chemistry: supplement vi. iupac subcommittee on gas kinetic data evaluation for atmospheric chemistry," J. Phys. Chem. Ref. Data **26**, 1329–1499 (1997).
53. R. Atkinson, D. Baulch, R. Cox, J. Crowley, R. Hampson, R. Hynes, M. Jenkin, M. Rossi, and J. Troe, "Evaluated kinetic and photochemical data for atmospheric chemistry: Volume iii–gas phase reactions of inorganic halogens," Atmospheric Chem. Phys. **7**, 981–1191 (2007).
54. M. Capitelli, C. M. Ferreira, B. F. Gordiets, and A. I. Osipov, *Plasma kinetics in atmospheric gases*, vol. 31 (Springer Science & Business Media, 2013).
55. G. Deffrennes, N. Jakse, C. M. Alvares, I. Nuta, A. Pasturel, A. Khvan, and A. Pisch, "Thermodynamic modelling of the ca–o system including 3rd generation description of cao and cao2," Calphad **69**, 101764 (2020).
56. S. L. Broadley and J. M. Plane, "A kinetic study of reactions of calcium-containing molecules with O and H atoms: implications for calcium chemistry in the upper atmosphere," Phys. Chem. Chem. Phys. **12**, 9094–9106 (2010).
57. R. Zhu, K.-Y. Lai, and M.-C. Lin, "Ab initio chemical kinetics for the hydrolysis of N_2O_4 isomers in the gas phase," The J. Phys. Chem. A **116**, 4466–4472 (2012).
58. R. Han, Y. Wang, S. Xing, C. Pang, Y. Hao, C. Song, and Q. Liu, "Progress in reducing calcination reaction temperature of calcium-looping CO_2 capture technology: A critical review," Chem. Eng. J. **450**, 137952 (2022).